Lawrence Berkeley National Laboratory

Title

Focused-helium-ion-beam blow forming of nanostructures: radiation damage and nanofabrication

Authors

Kim, Chung-Soo
Hobbs, Richard G
Agarwal, Akshay
et al.

Peer reviewed

Nanotechnology

Focused-helium-ion-beam blow forming of nanostructures: radiation damage and nanofabrication

Focused-Helium-Ion-Beam Blow Forming of Nanostructures: Radiation Damage and Nanofabrication

Chung-Soo Kim[1*], Richard G Hobbs[2*], Akshay Agarwal[1], Yang Yang[3], Vitor R Manfrinato[1], Michael P Short[3], Ju Li[3,4] and Karl K Berggren[1]

[1]Research Laboratory of Electronics, Massachusetts Institute of Technology, Cambridge, Massachusetts, 02139, United States

[2]School of Chemistry, Advanced Materials and Bioengineering Research (AMBER) Centre and Centre for Research in Adaptive Nanostructures and Nanodevices (CRANN), Trinity College Dublin, Ireland

[3]Department of Nuclear Science and Engineering, Massachusetts Institute of Technology, Cambridge, Massachusetts, 02139, United States

[4]Department of Materials Science and Engineering, Massachusetts Institute of Technology, Cambridge, Massachusetts, 02139, United States

Email: hobbsr@tcd.ie, berggren@mit.edu

Abstract

Targeted irradiation of nanostructures by a finely focused ion beam provides routes to improved control of material modification and understanding of the physics of interactions between ion beams and nanomaterials. Here, we studied radiation damage in crystalline diamond and silicon nanostructures using a focused helium ion beam, with the former exhibiting extremely long-range ion propagation and large plastic deformation in a process visibly analogous to blow forming. We report the dependence of damage morphology on material, geometry, and irradiation conditions (ion dose, ion energy, ion species, and location). We anticipate that our method and findings will not only improve the understanding of radiation damage in isolated nanostructures, but will also support the design of new engineering materials and devices for current and future applications in nanotechnology.

Introduction

Ion irradiation has been used extensively to tune the mechanical,[1–3] optical,[4–6] electrical,[4,6,7] and chemical[8,9] properties of materials, as well as for nanofabrication.[6,8,10–12] Understanding the response of materials to ion irradiation is especially important for the design of engineering materials, such as radiation-tolerant materials for nuclear reactors,[3,13–15] for ion implantation in semiconductors and for nanofabrication. In nanostructures, finely focused ion beams may play a critical role in locally modifying materials. For example, focused gallium ion beams (FGIB) have been used extensively for local modification of materials such as surface hardening,[2] wire straightening,[16] and nanowire growth.[17] Helium ion microscopy (HIM), facilitated by the development of gas field ion sources and sub-nanometer-diameter focused helium ion beams (FHIB), has opened up new avenues for imaging[18] and single-nanometer scale fabrication.[19] Potential impacts of HIM on nanoscience include nanometrology for critical dimension measurement,[20] biological imaging,[21] and nanofabrication for plasmonic antennas,[22] nanopores,[23] transmission electron microscopy (TEM) lamellae,[24] photomask repair,[25] and circuit editing.[26] Local modification of materials and defect creation *via* FHIB at the nanoscale has also been applied to quantum optics[27] and circuits.[28,29]

Understanding He_+ scattering in materials is critical to the use of FHIB to control material properties. In general, the distribution of FHIB-induced damage in materials depends on (1) the scattering ranges of helium in the material, (2) the sputtering yield and (3) helium solubility in the material. (1) Radial scattering and ion ranges of He_+ in materials are approximately twelve times

2

larger than that of Ga_+ with equivalent kinetic energy since the stopping power of He_+ is about twelve times lower than that of Ga_+. (2) The sputtering yield of He_+ is two orders of magnitude lower than that of Ga_+ for the materials studied in this work (carbon and silicon). This difference arises because He_+ loses energy primarily *via* electronic interactions with fewer atomic displacements than observed for Ga_+. Also, Ga_+-induced damage can reach a steady-state condition, resulting in a constant Ga_+ implantation profile by continuous surface recession due to sputtering.[30] (3) Helium has primarily repulsive interactions with host material atoms due to its closed-shell electron configuration and thus a low equilibrium solubility in the host material.[31] As a result, if kinetics allow, implanted He atoms can precipitate as He gas bubbles, which grow to dimensions equivalent to that of the He_+-exposed region. This bubble formation can lead to significant morphological changes such as surface swelling at ion doses of over 10^{17} ions/cm2.[32,33] If all three characteristics are considered, implanted He_+ may accumulate significantly within nanostructures, leading to gas bubble growth and "bloating" of targets without forming a steady-state radiation-damage profile. Simultaneously and unlike Ga_+, He_+ can scatter/diffuse and escape from irradiated targets into the surrounding vacuum by a process which we refer to as He_+ leakage. Consequently, He_+ may display a range of scattering behaviors in nanostructures resulting in both internal and surface damage to nanostructured targets (see figure S1 in the supplementary information for example).

Despite the physical understanding described above, details of the radiation effects due to FHIB have thus far only been investigated for a limited number of materials such as Si,[32,34,35] Cu,[32] Ni-Mo/Si,[25] TiO2[34], and graphene,[36] even though numerous other materials of interest exist. Diamond (crystalline carbon, hereafter referred to as c-C) is a particularly promising material in nanotechnology due to its extraordinary mechanical, optical, and thermal properties, and its

3

biocompatibility[37–39] for micro- and nano-electromechanical systems.[40,41] It is also of interest for quantum optics/computing, [42,43] magnetic resonance imaging (MRI),[44,45] and as an electron-optical material in new microscopy techniques such as quantum electron microscopy.[46] Therefore, there is considerable interest in understanding how c-C can be probed and modified using localized, targeted ion irradiation, for example a FHIB has been used to generate defects at controlled locations in diamond, which can subsequently be converted to luminescent nitrogen-vacancy centers for use in nanoscale MRI.[27,47]

In this work, we study the interaction of a FHIB with c-C nanostructures compared to those produced in crystalline silicon (hereafter referred to as c-Si). A new experimental approach to observe ion-nanostructure interactions in three dimensions (3D) is described, by preparing electron-transparent samples using FGIB and then characterizing FHIB-induced modifications in those samples both internally and externally by transmission and scanning electron microscopy (TEM and SEM), respectively. We investigated ion-nanostructure interactions as a function of material composition, ion dose, crystal orientation, substrate thickness, and ion energy. We observed nanostructure-specific physical phenomena, including anomalously long ion-penetration lengths and internal-gas-pressure-induced plastic deformation. We explain these phenomena by comparing material dimensions and morphologies measured by electron microscopy to Monte Carlo simulations. We used both SRIM[48] for ion-range prediction and Irradiation of Materials in 3D (IM3D)[49] to consider ion leakage effects in nanostructures. Furthermore, we have expanded our study to a new nanofabrication method for the production of 3D features through modification of existing micro- and nano-structures.

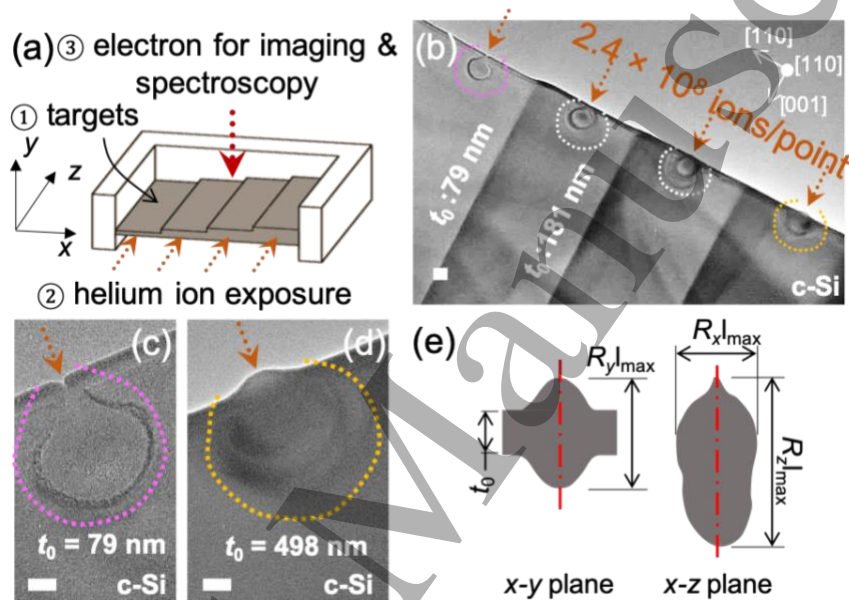**Method**

4

Figure 1a outlines our experimental approach to investigate FHIB effects on nanostructures and describes the three-step experimental procedure graphically. First, we used FGIB milling to prepare monocrystalline nanostructures with different geometries and crystal orientations on a TEM grid. Second, we irradiated targeted regions of the nanostructures under various conditions with a FHIB. Finally, we use TEM and SEM to observe He+-induced changes to internal and external morphologies, respectively. This method has advantages in that it provides direct 3D observation of site- and nanostructure-specific radiation damage without any post-processing of the specimens after ion irradiation. Previously, a similar method has been used, but no site- and nanostructure-specific damage was presented.[50] Using this experimental method, c-C nanostructures were the primary focus, while nanostructures of c-Si were chosen for comparison as there have already been a number of investigations of the response to c-Si to FHIB irradiation in both bulk and thin membrane forms.[32,51] Throughout the text we use a number of variables to correlate material properties (geometry and composition) and ion exposure conditions to observed changes in the materials. We have summarized these variables in Table 1. The supplementary material describes materials used, experiments, and measurements in greater detail.

Table 1. Summary of variables used in this work and the variables that they represent.

Variable	Definition
t_0	membrane thickness
D_0	ion dose
E_0	kinetic energy of ion
R_r	radial range of ion-induced damage in a homogeneous material
$R_x\|_{max}$, $R_y\|_{max}$, $R_z\|_{max}$	maximum range of ion-induced damage along x, y and z axes. In a homogeneous material, $R_x\|_{max} = R_y\|_{max} = 2 R_r$
$t_d\|_{max}$, $T_d\|_{max}$	$t_d\|_{max}$ represents the thickness of the deformed region *i.e.* $R_y\|_{max} - t_0$, which has a saturation value of $T_d\|_{max}$

P_{acc}, P_{acc}^{SRIM}, P_{acc}^{IM3D}	probability of helium ion coming to rest inside the nanostructure (P_{acc}) as calculated by SRIM (P_{acc}^{SRIM}) or IM3D (P_{acc}^{IM3D})
P_{esc}	probability of helium escaping from material *i.e.* 1- P_{acc}
p_i, $p_i|_{max}$	internal helium pressure within material (p_i) and maximum internal pressure at which higher order deformation proceeds
k	deformation resistance factor

Figure 1. Experimental method and examples of ion-nanostructure interactions in silicon. (a) Schematic of experimental method and procedure. (1) Preparation of electron transparent targets with different geometries (grey color) by FGIB and lift-out technique. (2) Targeted irradiation of nanostructures. (3) Characterization by electron microscopy. (b) TEM image of c-Si membranes with different thicknesses irradiated with 35 keV He+ as illustrated in (a). A point-exposure delivered $2.4 \times 10_8$ ions/point to each membrane in the direction of the orange arrows. (c-d) Higher magnification TEM images when membrane thickness $t_0 = 79$ nm and $t_0 = 498$ nm in (b). The former shows removed volume and the latter shows swelled volume at the FHIB entry point as indicated by the orange arrows. (e) Measured parameters ($R_{x,y,z}|_{max}$) for He+-exposed membranes viewed normal to the *x-y* plane (SEM) and the *x-z* plane (TEM). White scale bars represent a length of 100 nm.

Results and discussion

6

In this work, we studied interactions between a FHIB and c-C and c-Si nanostructures as a function of various parameters, including ion-exposure method (single point or scanned), exposure location, ion dose (D_0), ion energy (E_0), nanostructure geometry, and ion species. Figure 1 provides an overview of our approach and a summary of the damage observed in silicon samples for comparison to diamond in subsequent figures. In figures 1b-d we consider the interactions of a FHIB with c-Si membranes that were fabricated with different thicknesses (t_0). Comparing figures 1c and 1d, we see significant surface swelling at the point where the FHIB enters the 498 nm thick membrane, which is absent from the 79-nm-thick membrane. This comparison implies that FHIB-induced damage depends on sample geometry as is also seen in the case of c-C and discussed later in figure 5. Figure 1e shows how we measured FHIB-induced damage in a thin membrane using electron microscopy. The maximum lateral range of damage along the x-axis, termed $R_x|_{max}$ and longitudinal range along the z-axis, termed $R_z|_{max}$ was measured in the x-z plane, along with the maximum volume deformation along the y-axis in the x-y plane, $R_y|_{max}$. In a homogeneous medium, $R_x|_{max}$ and $R_y|_{max}$ are expected to be equal and would both be estimated as twice the radial distribution range R_r (measured from the optical axis), due to the axial symmetry of He_+ scattering in a bulk homogeneous solid. In our case, we must treat $R_x|_{max}$ and $R_y|_{max}$ differently, because damage is formed differently along the x- and y-axes. Thus, $R_x|_{max}$ was comparable to $2R_r$ and $R_y|_{max}$ was used to estimate the observed volume deformation. We use these measured values as well as others listed in table 1 to explain results related to FHIB-induced damage in this work.
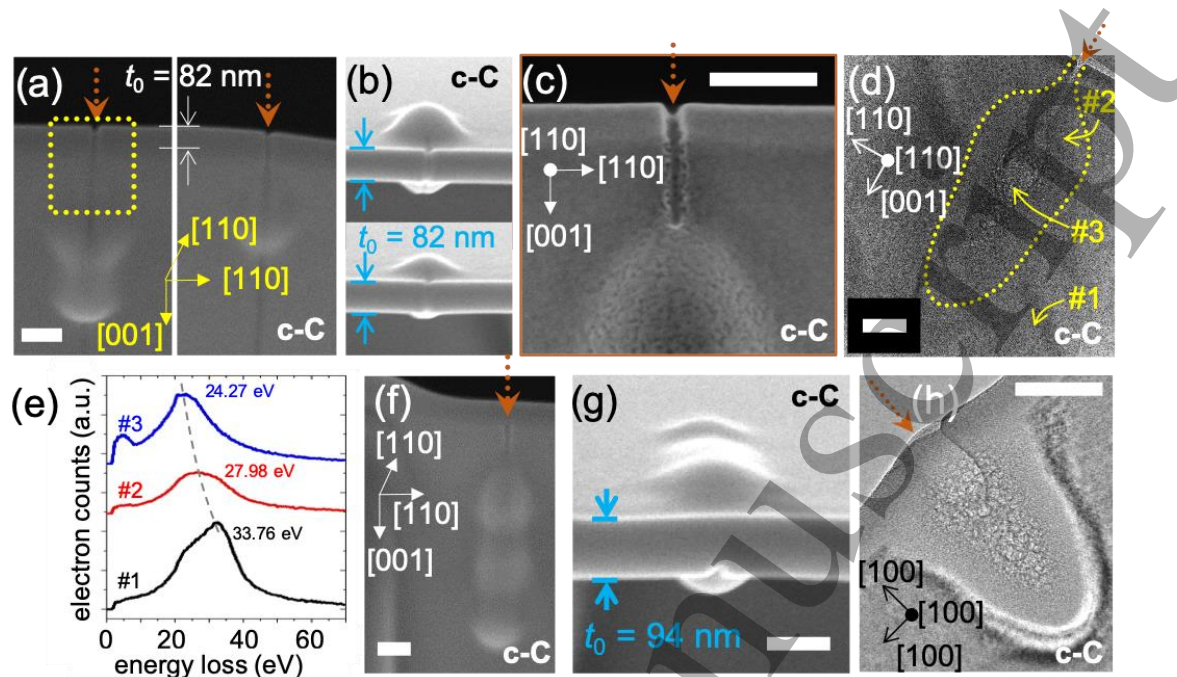
Figure 2. Examples of ion-nanostructure interactions in diamond (c-C). (a-b) SEM images of 82-nm-thick c-C membranes exposed to 35 keV He+. A line-exposure along the *y*-axis delivered 2.4 $\times$ 10$_8$ (left) and $4.0 \times 10_7$ ions/line (right). Damage observed in (a) and (b) was viewed at angles of 52° and -10°, respectively, and shows dose-dependent volume deformation. (c) Magnified SEM image of region in yellow box in (a) shows a sputtered volume and a roughened surface. (d) TEM image of left side of sample in (a) showing internal He+-induced damage within the region outlined by the dashed line. (e) EELS spectra showing the shift in energy of volume plasmon peaks, sampled from three points in (d). Peaks at 33.76 eV, 27.98 eV, and 24.28 eV in curves #1 to #3 resulted in calculated densities of 3.47 g/cm$_3$, 2.38 g/cm$_3$, and 1.79 g/cm$_3$. (f-g) SEM images of 94-nm-thick c-C membranes exposed to 35 keV He+ with a dose of $2.4 \times 10_8$ ion/point and the same crystal orientation as in figures a-b. He+ point-exposure was applied at the edge of the membrane on the *x-y* plane. Images show three volume deformations. (h) TEM image of 87 nm thick c-C membrane exposed to 10 keV He+ with a dose of $8.0 \times 10_7$ ion/point. Surface sputtering and gas bubble formation are observed. White scale bars represent a length of 100 nm.

Figure 2 summarizes the observed interactions between a FHIB and c-C membranes. Figures 2a-b show the surface of an 82-nm-thick c-C membrane after irradiation by a linear scan with a FHIB at two different doses and shows that more FHIB-induced damage occurred along the *x*- and *z*-directions when a higher dose was applied. The observed swelling orthogonal to the beam direction

8

was not always seen in previous reports,[35] as it would have been destroyed during preparation of the TEM sample except in the case of the methods used in references 3 and 10. Volumetric deformation seen in figures 2a-b is indicative of dose-dependent FHIB-induced damage. Furthermore, comparison of these results with those for c-Si shown in figures 1b-d highlights the additional material dependence. Figure 2c is a magnified image of the yellow boxed region in figure 2a and shows that our method enables observation of changes in surface morphologies due to nanoscale sputtering. Figure 2d displays a TEM image of the damaged region within the nanostructure presented at the left side in figure 2a. This figure shows the internal structure of the region irradiated by the FHIB, including longitudinal damage extending 634 nm below the surface. The depth of the longitudinal damage is larger than the 146 nm ion-penetration depth predicted by SRIM for 35 keV He_+ in c-C, which will be considered in further detail in discussions of figure 3. Figure 2e shows the results of electron energy-loss spectroscopy (EELS) analyses, where a shift in the energy of volume plasmon peak of c-C was observed and attributed to FHIB-induced damage. The volume plasmon energy depends on the density of the material and as such we used the shift in volume plasmon energy to estimate the change in density of the material due to interactions with the FHIB.[52] We estimated a density reduction of approximately 50% going from pristine c-C (3.47 g/cm_3) to damaged diamond (1.79 g/cm_3). The supplementary information describes how the estimation of density using EELS was conducted. Figures 2f-g show the external structure of a 94-nm-thick c-C membrane after a FHIB point exposure at the edge of the membrane. The longitudinal damage range observed is 938 nm, which is approximately 300 nm larger than the value shown in figure 2d. This comparison implies that FHIB-induced morphology changes depend on exposure method and location. Figure 2h shows a TEM image of a 87-nm-thick c-C membrane exposed to a 10 keV FHIB using a point-exposure at the center of the membrane. Strong

9

surface sputtering was observed near the point where the FHIB entered the sample as He_+ loses more energy via nuclear interactions at 10 keV relative to 35 keV. Nuclear losses for 10 keV and 35 keV He_+ in c-C are 23.24 eV/Å and 10.43 eV/Å respectively as calculated by SRIM.

The results shown in figures 1 and 2 summarize the FHIB-induced damage in c-Si and c-C observed in this work and demonstrates that our method enables detailed observation of this damage. In the following sections, we will describe the results of targeted FHIB irradiation in c-Si and c-C nanostructures with respect to dose (D_0), membrane thickness (t_0), crystal orientation, and ion energy (E_0).

Figure 3 presents the results of our investigation of the effect of FHIB dose (D_0) and material (c-C *vs.* c-Si) on FHIB-induced morphology changes using membranes having similar thicknesses (t_0). In order to study the effects of dose and composition, we prepared membranes from c-C and c-Si with t_0 of 73 nm and 71 nm, respectively. Each membrane used had the same crystal orientation ($\hat{x} = \hat{y} = [110]$ and $\hat{z} = [001]$). We performed a point-exposure with 35 keV He_+ at a central position on the membrane, normal to the *x-y* plane of each membrane, with five different values of D_0 (8.1 $\times$ 10_6, 4.1 $\times$ 10_7, 8.1 $\times$ 10_7, 1.6 $\times$ 10_8, and 2.4 $\times$ 10_8 ions/point), where each point has an effective focal area of about 1 nm_2.

Figures 3a-b show representative results observed by TEM in c-C and c-Si, respectively ($D_0 = 2.4 \times 10_8$ ions/point). These images show the apparent boundary between damaged and undamaged regions in c-C and c-Si. Specifically, c-C exhibits an extended damage range along the *z*-axis ($R_z|_{max} = 857$ nm) with three peaks in R_x observed moving along the *z*-axis and increased gas bubble formation, *e.g.* nanobubbles and clusters thereof, which we refer to as bubble clusters. In the case of c-Si, the damaged region shown in figure 3b is similar to the damaged region reported

10

in previous studies with bulk c-Si substrates.[33,51] However, in those works only nanobubbles were observed in c-Si even though the applied dose exceeded that required for bubble cluster formation (D_0 of 10^{17} ions/cm^2).[32] We will discuss the reported absence of bubble clusters later in the text when we discuss ion leakage effects. Figures 3c-d show SEM images of FHIB-exposed c-C and c-Si, respectively ($D_0 = 2.4 \times 10^8$ ions/point). These images show external damage in the form of volume deformation. Specifically, c-C exhibits extended damage with a measured $R_y|_{max}$ value of 240 nm, which is 1.6 times larger than $R_y|_{max}$ for c-Si. The increased gas bubble formation seen in c-C is likely to promote volume deformation as seen in previous reports for Si and Cu.[32,33,53]
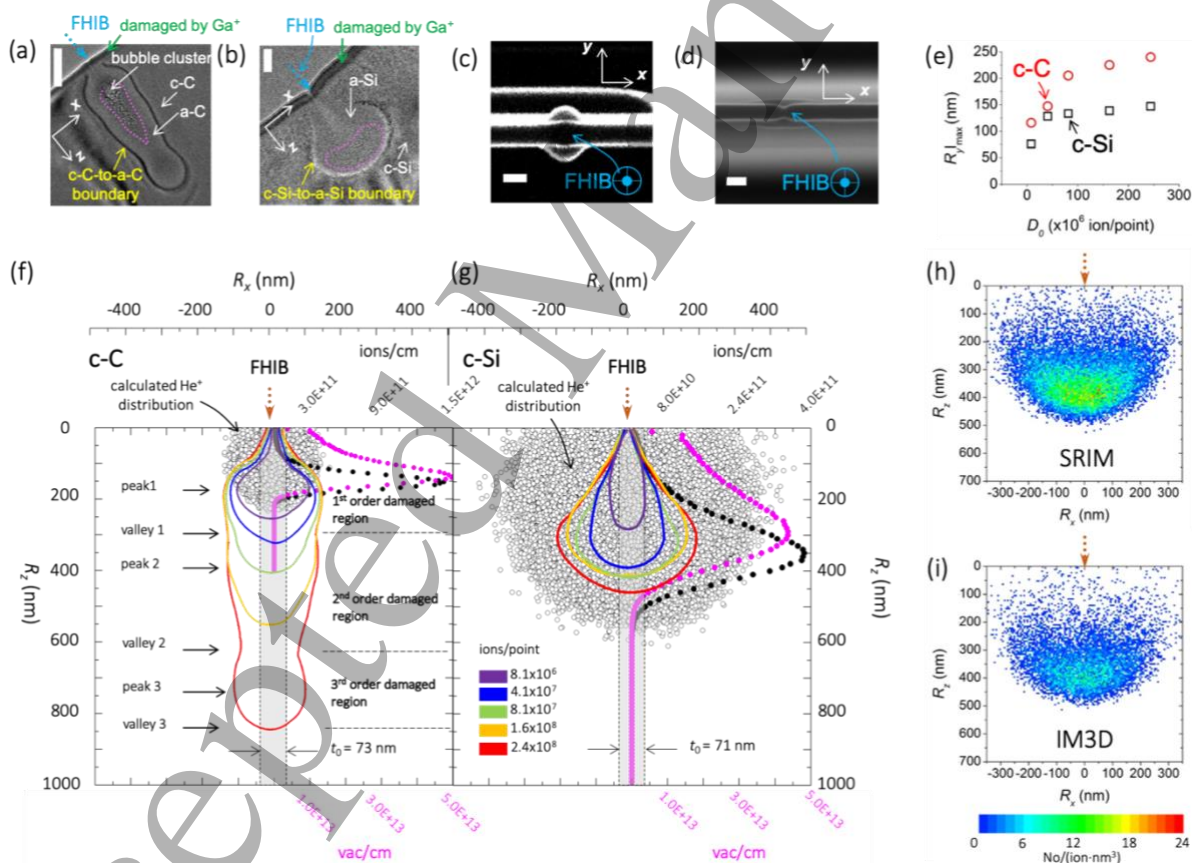
Figure 3. He+-induced damage in c-C and c-Si as a function of D_0. White scale bars in (a-d) are 100 nm. (a-b) TEM images of (*x-z plane*) He+-exposed c-C membranes (a) and c-Si (b) (ion dose = 2.4×10^8 ions/point). The boundaries between crystalline and amorphous regions in c-C and c-Si are distinguishable. Measured $R_z|_{max}$ for c-C and c-Si are 857 nm and 433 nm, respectively. Pink

11

dotted lines in each figure show the boundary of regions where gas bubbles formed. (c-d) SEM images of the surface morphology (x-y plane) of He+-exposed c-C (c) and c-Si (d) membranes in the same samples as (a-b). Measured $R_y|_{max}$ for c-C and c-Si are 240 nm and 147 nm, respectively. (e) Measured $R_y|_{max}$ for c-C and c-Si (x-y plane) as a function of D_0. (f-g) Profiles of He+-induced damage in c-C and c-Si (x-z plane) as a function of D_0, obtained from TEM images. Distribution of He+ projected in the x-z plane, He+ density (ions/cm) and vacancy density (vac/cm) along z-axis, calculated from SRIM are overlaid (black and magenta dots respectively). The final locations of He+ were projected onto the x-z plane. He+ and vacancy densities were calculated using $D_0 = 8.0 \times 10^6$ ions/point. In c-C (f), three peaks and troughs in the width of the damaged region are observed moving along the z-axis (red trace) for $D_0 = 2.4 \times 10^8$ ions/point. Increasing numbers of peaks and troughs emerge with increasing dose. These peaks and troughs are used to define higher order damages regions as shown. Virtual membranes (y-z plane) with t_0 of 73 nm for c-C (f) and 71 nm for c-Si (g) are overlaid to show He+ leakage due to the membrane geometry. (h-i) 2D He+ distribution on the x-z plane at the center of the y-axis in c-Si without (h) and with (i) consideration of finite membrane thickness ($t_0 = 73$ nm) using IM3D.

Figure 3e summarizes the observed trends in measured values of $R_y|_{max}$ as a function of D_0 for c-C and c-Si. $R_y|_{max}$ is larger for c-C than for c-Si and increases in both materials with D_0. The larger values of $R_y|_{max}$ in c-C relative to c-Si are consistent with the larger lattice parameter in c-Si, which supports an increased probability of helium escape for c-Si, while the increase in $R_y|_{max}$ with ion dose is expected based on the decrease in material density during damage formation and helium accumulation within the material. Figures S2-4 in the supplementary material show micrographs for other values of D_0. Figures 3f-g summarize the evolution of damaged regions in the x-z plane as a function of D_0 with profiles of the damaged regions observed in TEM images of c-C and c-Si represented by solid colored lines. Figures 3f-g also include three SRIM simulation results, He+ distribution projected in the x-z plane, and densities of He+ and vacancies along the z-axis. The supplementary material describes SRIM simulations in detail. Plotted densities of He+ and vacancies were calculated using the minimum D_0 of 8.1×10^6 ions, because SRIM does not account for dynamic processes such as density reduction and gas bubble formation observed at higher doses.[10,48,52] Thus, comparison of experimental and simulation results is reasonable at doses

12

of $8.1 \times 10_6$ ions where bubbles are not formed in both materials. The simulated He_+ distribution maps differ from experimental profiles in both c-C and c-Si. The simulated densities of He_+ and vacancies along the z-axis show only a single peak in both c-C and c-Si, while in experiments c-C exhibited multiple peaks. In figure 3f, we describe the multiple peaks and valleys in the boundary between amorphous and crystalline material along the z-axis as separating N_{th}-order damaged regions. These labels will be used when discussing long-range ion propagation below. We determined the locations of peaks and valleys by observing the widest and narrowest $R_x/_{max}$ values.

The material dependence of ion-induced damage and deformation observed is related to the thickness of the nanostructures. This dependence occurs because the calculated radial damage range (R_r) in each material is larger than half the membrane thickness $t_0/2 \cong 37$ nm, and so helium can escape from the material in a process that we term "ion leakage". The calculated values of R_r for c-C and c-Si using SRIM are 40.9 ± 21.5 nm and 145.3 ± 70.8 nm, respectively. Figures 3f-g show the effect of membrane geometry by overlaying two grey-colored bars on simulation and experimental results representing membrane thickness. Inspection of the simulated He_+ distribution with respect to t_0 suggests that more He_+ scatters out of a virtual membrane in c-Si than in c-C, likely due to the reduced stopping power of 35 keV He_+ ions in c-Si (11.6 eV/Å) compared to c-C (29.8 eV/Å).

We quantified the number of He_+ ions coming to rest inside the membrane as the probability of He_+ accumulation (P_{acc}), where the probability of escape was $P_{esc} = 1 - P_{acc}$ for a given t_0. The resulting values calculated using SRIM $P_{acc}^{SRIM} = 0.73$ (c-C) and $P_{acc}^{SRIM} = 0.23$ (c-Si). This result indicates that the probability of He_+ trapping is 3.17 times larger in c-C than in c-Si due to larger loss of He_+ kinetic energy per collision in c-C (m_{He} is closer to m_C than m_{Si}). This trapping contributes not only to gas bubble nucleation, but also to subsequent collision cascades between

13

incident primary ions and trapped helium, resulting in additional radiation damage in c-C, where the probability of ion leakage is lower than in c-Si. However, this SRIM calculation includes He_+ recoil back into the nanostructure, which cannot happen once the He_+ has left the film, as SRIM cannot handle real 3D geometries.[54] Thus, we performed a full 3D Monte Carlo simulation using IM3D, which accounts for the leakage of He_+ in arbitrary 3D geometries. The simulated probabilities for accumulation using IM3D, P_{acc}^{IM3D}, were 0.69 and 0.08 in c-C and c-Si, respectively. Thus, the IM3D simulation results differ significantly from those obtained from SRIM.

Given the high P_{acc} in c-C, gas bubbles and atomic displacements are more probable in c-C than in c-Si. This increase in damage results in $R_y|_{max}$ in c-C being 2.25 times larger than that in c-Si at the maximum D_0, as shown in figures 3c-e. The supplementary material describes the calculation of P_{acc} and P_{esc} in detail. Figure S5 in the supplementary material shows P_{acc} as a function of t_0 for both c-C and c-Si.

The ion leakage effect enables us to explain the absence of bubble clusters in c-Si (figure 3b) at $D_0 = 2.4 \times 10^8$ ions/point, equivalent to 2.4×10^{22} ions/cm2, since each point has an effective area of about 1 nm2. This areal dose density is four and five orders of magnitude higher than the nucleation doses for nanobubbles and bubble clusters, respectively.[32] We would thus naively expect bubble clusters to form. By accounting for dose from the proximity effect and P_{acc}, the effective D_0 in figure 3b reduces to about 1.7×10^{17} ions/cm2 (SRIM) or 6.1×10^{16} ion/cm2 (IM3D). The effective D_0 obtained using IM3D is thus below the nanobubble nucleation dose of 10^{17} ions/cm2 reported in previous work.[32] While estimates of bubble nucleation dose thresholds are admittedly inexact, the fact that bubbles are indeed not observed does support the notion that IM3D describes ion-nanostructure interactions more accurately than SRIM.

14

Additionally, we provide an example of the necessity for consideration of He_+ leakage when computing ion-solid interactions, in figures 3h-i. The distributions calculated by SRIM (figure 3h) differ significantly from those calculated by IM3D (figure 3i). As IM3D accounts for the three-dimensional structure of the system, while SRIM does not, we presume figure 3i gives a more accurate estimate of the actual behavior of the process.
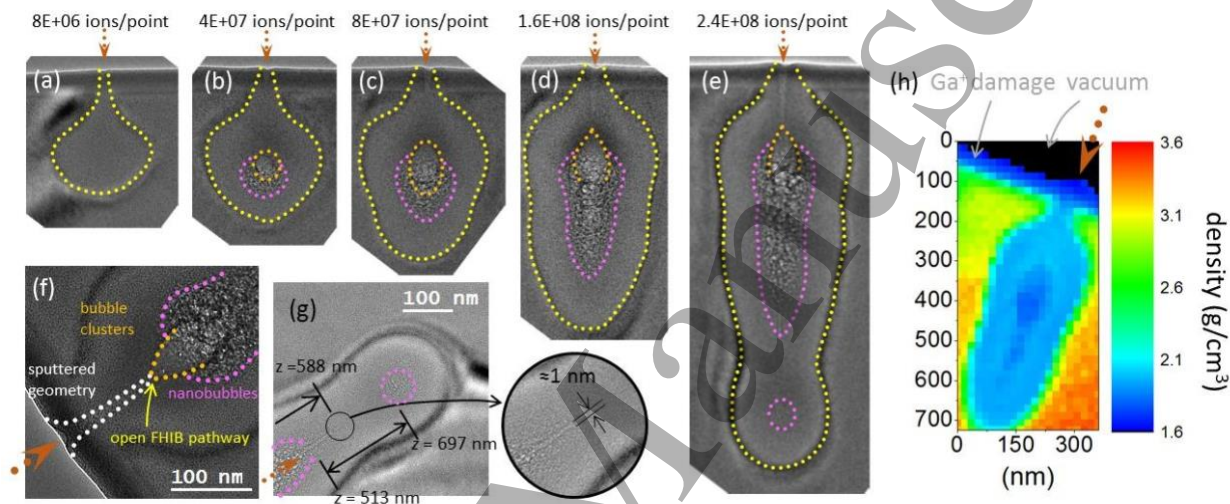
Figure 4. Evolution of long-range ion-propagation with increasing ion dose. TEM images in (a-e) were used to form the contours shown in figure 3f. The dotted brown arrow indicates the direction of the incident FHIB. Yellow dashed lines, drawn by hand, mark the crystal-to-amorphous boundary in the material. This boundary forms a geometric constraint as explained in the text. (a) TEM image shows the damaged amorphous region without gas bubbles. (b) TEM image shows the onset of nucleation of nanobubbles (dashed pink line) and bubble clusters (dashed orange line). (c-d) TEM images show the onset of the 2_{nd} order damaged regions (as defined in figure 3f) with extended nanobubble formation along the z-axis. (e) TEM shows further extended He_+ propagation, resulting in a 3_{rd} order damaged region ($R_z|_{max} = 857$ nm). (f) TEM image shows the connection between the sputtered volume and bubble clusters, which act as an exit for helium gas and an entrance for the FHIB into the newly formed cavity. A white dotted line shows the geometric boundary of the sputtered volume. (g) Image shows a magnified view of a region 588 nm beneath the surface shown in figure 4e. This image shows ultra-fine features with 1-nm lateral extent inside the membrane. (h) 2D density map, calculated using the volume plasmon energy measured by EELS. The specimen used here is shown in figure 2a. The measured sample density had a range of 1.72-3.47 g/cm3. The region where helium gas bubbles formed showed the lowest density values.

15

Figure 4 describes the evolution of long-range ion propagation in c-C as a function of D_0. The damaged region at the lowest D_0 of 8×10^6 ions/point in figure 4a does not include bubbles, which indicates that the $R_y|_{max}$ measured in figure 3e first occurred by a phase transition from c-C to amorphous carbon (a-C). We compare the vacancy density calculated in figure 3f with the threshold vacancy density of $1\text{-}9 \times 10^{22}$ vac/cm^3 required to convert c-C to a-C under broadband helium ion implantation,[52,55] due to the absence of existing experimental data using focused beams with c-C. Applying the proximity effect and P_{acc} corrections as before, the reduced vacancy densities are about 7.3×10^{22} vac/cm^3 (SRIM) and 6.9×10^{22} vac/cm^3 (IM3D). These values are consistent with the threshold vacancy density from the literature mentioned above.

The transition to an amorphous state not only leads to lower density, but also forms a geometric constraint at the interface between the amorphous and crystalline phases of the material where the rigid crystalline material constrains the ductile amorphous material. The yellow dashed line in figure 4a shows the boundary of the geometric constraint, which evolves with increasing He$_+$ irradiation dose as shown in figures 4b-e. When the damaged amorphous region extends along the y-axis to the surface (*i.e.* when $t_0 < R_y|_{max}$), the surface is readily deformed resulting in the observed 'bloating', an effect we take advantage of below as part of the "blow forming" process. This bloating occurs because there is no longer a c-C layer at the surface acting as a geometrical constraint to the ductile amorphous material.

To establish the local material density in FHIB-irradiated c-C, we used electron energy loss spectroscopy (EELS). The estimated average density in a-C ($\rho_{a\text{-}C}$) was 2.04 g/cm^3 (figure S6), which indicates a 42% drop in density relative to c-C. This $\rho_{a\text{-}C}$ of 2.04 g/cm^3 is close to that expected for stable amorphous allotropes of carbon having densities of 2.06-2.35 g/cm^3, measured after ion implantation and micro-beam irradiation at 50-500 keV with various ion species.[52,55,56]

16

The reduction in density also implies a drop in the elastic modulus and the material becomes more ductile as a-C is formed.[55,57]

It is also notable that the simulated He+ distribution in c-C closely matched the observed damaged region in the experiment at the lowest D_0 of 8×10^6 ions/point, as shown in figure 3f, presumably because the nucleation of gas bubbles did not occur and ion leakage in c-C was not significant.

Figures 4b-e show the formation and development of nanobubbles in c-C. Figure 4b shows the onset of both nanobubbles and bubble clusters at D_0 of 4×10^6 ions/point. Above this dose, volume deformation is likely to be induced by gas bubble formation as the internal pressure, p_i, increases in the membrane (figures 4c-e). Figure 4c shows the growth of helium bubbles within a 1st order damaged region and at the onset of 2nd order damage. Figure 4d shows the continuation of those two processes with additional FHIB irradiation. The onset of 2nd order damage results from increased helium and vacancy accumulation deeper within the sample and thus greater helium penetration as scattering is reduced in the lower density material formed by accumulation of helium and vacancies. A region of 3rd order damage is observed in figure 4e at a dose of 2.4×10^8 ions/point. The 3rd order region is separated from the 2nd order region by a bubble-free region at $z = 513$ nm. The disappearance of nanobubbles in this region may be due to helium release, which can occur due to the rupture of deformed surfaces by high-pressure gas bubbles.[53] In this case, the helium gas may release through the entrance channel that formed due to sputtering and bubble clusters, as shown in figure 4f. Therefore, He+ can propagate through the formed internal cavity until it strikes sub-surface vacuum-carbon interfaces.

Figure 4g shows evidence of long-range FHIB propagation as a remnant of an ultra-fine FHIB (≈ 1 nm lateral width) is observed at $z = 588$ nm. This long-range FHIB propagation is likely

17

responsible for creating the 3rd order volume deformation. The depth of field of FHIB is estimated to be ~ 1 μm based on the image resolution (1 nm) and the beam convergence angle (1 mrad)[58], and supports this observation.

We have shown that FHIB exposure of c-C results in damage to the material and an associated decrease in material density. Here, we estimate changes in the density of FHIB-irradiated c-C membranes containing gas bubbles using EELS. Figure 4h shows a measured 2D density map with densities ranging from 1.72-3.47 g/cm^3. Based on the maximum density of a-C (2.95 g/cm^3) measured in reference 49, we divided the measured densities into two ranges: c-C for densities of 2.96-3.47 g/cm^3 and a-C for 1.72-2.95 g/cm^3. Figures S7-S8 in the supplementary material shows more detailed density maps. Specifically, the density near nanoscale voids is lower than that expected for stable carbon allotropes (2.15-2.35 g/cm^3). A density of less than 2.15 g/cm^3 supports plastic deformation in highly damaged regions (a-C) as observed in figures 2-4. A density less than that of stable allotropes caused by FHIB irradiation could occur due to tensile strain, which in turn leads to volume deformation, nanobubble formation, and transmission milling.[51,59] These combined phenomena appear on the outer surface in figure 2c. Additionally, secondary sputtering by scattered ions and sputtered C atoms inside the membrane may also play a role. EELS analysis also revealed a peak in the 4-8 eV energy-loss range for a-C (figures 2e and S9). This peak is associated with sp_2-hybridized carbon, shifting to lower energy and increasing in intensity with proximity to the path of the primary ion beam. Charged-particle beams have previously been used to convert sp_3 allotropes of carbon into sp_2 carbon, which is consistent with our observations.[52,60]

18
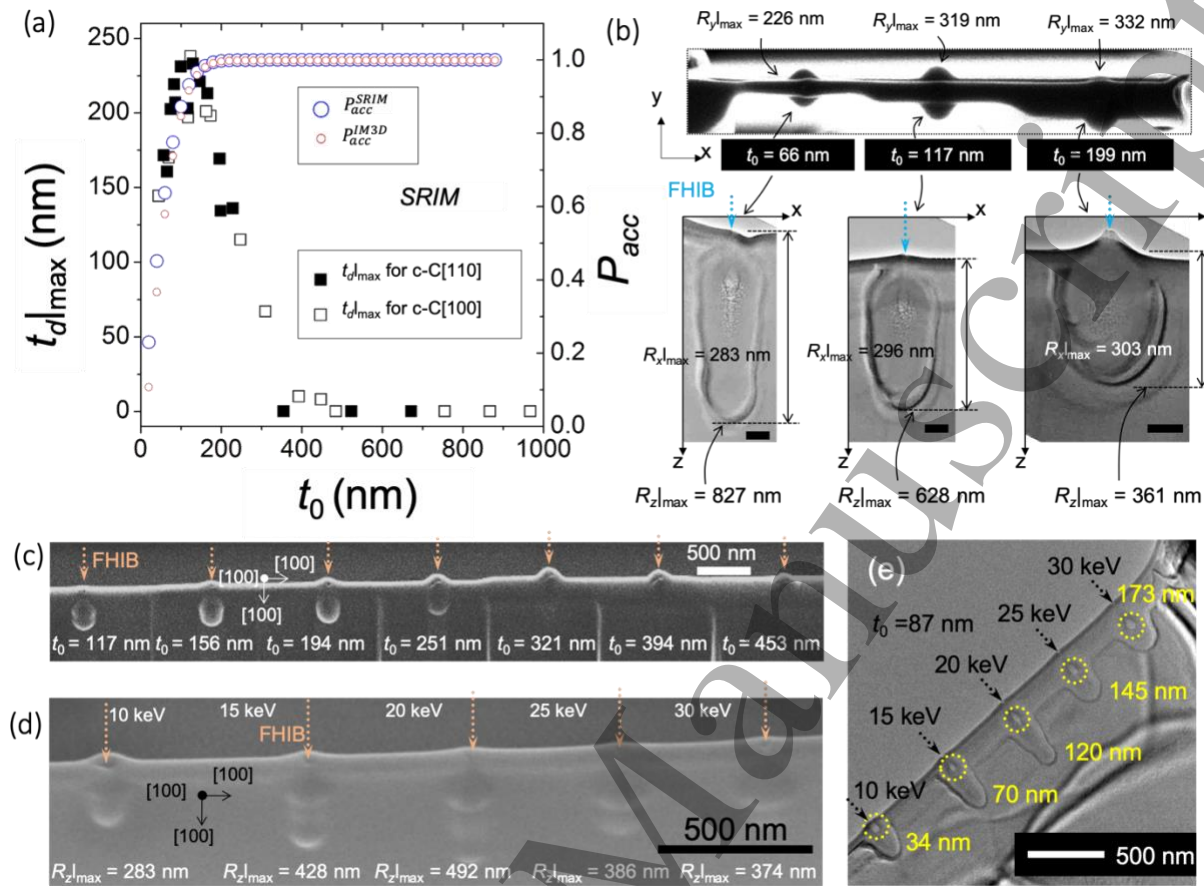
Figure 5. He+-induced damage in c-C as a function of t_0 and E_0. All dotted arrows represent locations and directions of the incident FHIB. (a-c) Influence of He+-induced damage as a function of t_0. A point exposure method was used to irradiate a point at the center of membranes with a 35 keV FHIB and D_0 of 2.4×10^8 ions/point. (a) We measured $t_d|_{max}$ versus t_0. ■: $t_d|_{max}$ of c-C[110], □: $t_d|_{max}$ of c-C[100], and P_{acc}, calculated from SRIM(○) and IM3D(○), as a function of t_0 is overlaid. Both materials show similar changes in $t_d|_{max}$, and t_0 has a significant effect on $t_d|_{max}$. (b) Top: SEM image of exposed c-C[100] recorded normal to the *x-y* plane. Bottom: TEM images of exposed c-C[100] recorded normal to the *x-z* plane. Measured $R_y|_{max}$ and $R_z|_{max}$ for three different values of t_0 of 66 nm, 117 nm, and 199 nm are indicated. Both $R_z|_{max}$ and gas bubble formation are reduced as t_0 increases. Black scale bars are 100 nm. (c) SEM image showing more test specimens exposed to He+ as in (a-b). Volume deformation along the *z*-axis decreases with t_0 and upward volume deformation dominates for $t_0 > 194$ nm. (d-e) Influence of E_0 on He+-induced damage. An 87 nm thick c-C[100] membrane was exposed with a fixed ion dose of 8×10^7 ions/point. SEM (d) and TEM (e) images show external and internal damage, respectively. In (e), dotted yellow circles and numbers represent locations of gas bubble clusters along the *z*-axis and their maximum lateral width, respectively. Damage appearing along the *z*-direction did not increase linearly with E_0.

19

Figure 5 summarizes the results of our study of the effects of material thickness and ion energy on FHIB-induced damage in c-C. We considered two crystal orientations, $\hat{x} = \hat{y} = [110]$ and $[100]$ in this work (crystal orientation was observed to have a negligible effect on the magnitude of deformation). Hereafter, each is referred to as c-C[110] and c-C[100]. A variety of values of t_0 ranging from 60 nm to 1 μm was considered for each crystal orientation. We define the deformed thickness $t_d|_{max}$ for each membrane as the difference between $R_y|_{max}$ and t_0. Most membranes were prepared from bulk c-C substrates, and some membranes were prepared on a TEM grid for subsequent analysis by TEM. A 35 keV FHIB was used to expose the center of samples with a fixed D_0 of $2.4 \times 10_8$ ions/point. Figures S10-13 show the collected micrographs for all relevant experimental results.

Figures 5a-c show the effect of t_0 on the deformation. Figure 5a shows the measured $t_d|_{max}$ for c-C[110] and c-C[100] as a function of t_0, which clearly shows that $t_d|_{max}$ depends on thickness, while crystal orientation has a negligible effect. Figure 5b shows SEM (top) and TEM (bottom) images in x-y and x-z planes for He+-exposed c-C[100] for three different values of t_0. Figure 5c shows more experimental results of He+-exposed c-C[100] inspected by SEM. As t_0 increases, figure 5a shows that the magnitude of deformation, $t_d|_{max}$, first increases and then decreases, and figures 5b-c shows that $R_z|_{max}$ decreases monotonically.

The behavior of $t_d|_{max}$ in figures 5a-c is presumably a consequence of the maximum internal pressure ($p_i|_{max}$) that can build up inside membranes for the 1_{st} order volume deformation before allowing higher order deformation. We define a deformation resistance factor k to determine $p_i|_{max}$. The parameter k may have the same form of flexural rigidity for the case of a circular flat plate subjected to uniform pressure with a clamped edge.[61] This is valid if we assume that pressurized regions are constant as a circular shape in the x-y plane at the 1_{st} order damage region and materials

20

are homogeneous in all experiments. Then, k is simply a monotonically increasing function of t_0, because a thicker membrane will be more difficult to deform under a constant pressure. Consequently, we can summarize three important points as follows: (1) $p_i|_{max}$ scales with k to a maximum value, which is equivalent to that of a bulk sample. (2) p_i increases with the product of dose and the probability of helium accumulation ($D_0 \cdot P_{acc}$). (3) $t_d|_{max}$ will reach a maximum deformation $T_d|_{max}$ when $p_i = p_i|_{max}$. Additional pressure above $p_i|_{max}$ will contribute to the creation of higher order damage regions and volume deformation.

The quantitative estimation of k is not considered in this work for two reasons: (1) Material properties of membranes change dynamically and are non-homogeneous, as shown in figure 4h. (2) An increase in the surrounding volume of c-C relative to a-C produced by He+ irradiation leads to different boundary conditions at each t_0. Specifically, when $t_0 \geq 2R_r$, a composite bi-layer will be formed consisting of a-C (interior) and c-C (exterior), which will lead to a change in mechanical properties, as the elastic modulus of c-C is of the order of ten times larger than that of a-C.[57]

In summary, we can best explain the effect of thickness on $t_d|_{max}$ by subdividing the thickness into three different regimes (see figure 5a) as follows. In the first regime, ($t_0 \leq 130$ nm), material deformation increases as t_0 increases. This increase is consistent with an increase in P_{acc} with increasing thickness. As t_0 increases, there is less helium leakage and more helium accumulates in the nanostructure resulting in greater deformation. In the second regime, where 130 nm $\leq t_0 \leq 375$ nm, $t_d|_{max}$ decreases as t_0 increases. At larger value of t_0, the a-C region formed by the FHIB no longer extends all the way to the surface of the membrane along the y-axis. Consequently, a c-C layer exists at the surface that acts to constrain the ductile a-C and reduce deformation. This c-C layer increases in thickness as t_0 increases and thus reduces deformation. In the third regime where $t_0 \geq 375$ nm, no change in $t_d|_{max}$ is observed at all. We interpret this as a

21

micro-to-bulk transition, implying that the materials response to ion irradiation can be regarded as that of the bulk material ($k = 1$).

Unlike $t_d|_{max}$, $R_z|_{max}$ decreases monotonically with increasing t_0 before reaching a minimum at value when $t_0 > 375$ nm. This suggests that the reduction in material density along the ion-beam axis is lower in thicker samples for a given dose, which is consistent with an increase in k with increasing thickness. This implies that the rate of increase of k with respect to t_0 is larger than that of $D_0 \cdot P_{acc}$. If it were not, $R_z|_{max}$ would follow the same trend as that of $t_d|_{max}$ with increasing t_0. The rapid increase of k with t_0 implies that k is very small when $t_0 < 2 \cdot R_r$. This prediction is reasonable because c-C membranes can be fully amorphized in the y-z plane for $t_0 < 2 \cdot R_r$. In fact, the longest $R_z|_{max}$ of 827 nm was observed when $P_{acc} = 0.6125$ at $t_0 = 66$ nm. Additionally, when $t_0 > 130$ nm, volume deformation also occurred in an upward direction, as shown in figures 5b-c. This upward volume deformation is a result of deformation toward the weakest part of the FHIB-damaged area with stress concentration at the sputtered point of incidence of the FHIB. The upward volume deformation is typical of FHIB interactions with bulk materials.[32,33]

The measured $R_x|_{max}$, $R_y|_{max}$ and $R_z|_{max}$ are similar for both crystal orientations studied. For instance, c-C[100] with t_0 of 66 nm exhibited $R_x|_{max}$, $R_y|_{max}$ and $R_z|_{max}$ values of 266 nm, 226 nm, and 827 nm, respectively (figure 5b). These values are comparable to c-C[110] where t_0 was 73 nm (figure 3b) and $R_x|_{max}$, $R_y|_{max}$ and $R_z|_{max}$ were 272 nm, 240 nm, and 854 nm, respectively. The negligible effect of crystal orientation is likely related to the high He+ dose, which collapses any anisotropy in mechanical properties and material density. In other words, a D_0 of $8.1 \times 10_6$ ions/point was sufficient to convert c-C to a-C, as shown in figure 4a. The FHIB-induced conversion of c-C into amorphous carbon is likely to suppress ion channeling, which would exhibit a dependence on crystal orientation. Figure 5a also shows calculated P_{acc}^{SRIM} and P_{acc}^{IM3D} as a function

22

of t_0. As t_0 increases, both values increased and are comparable with less than a 2% difference when $t_0 \geq 120$ nm.

In figures 5d-e, we show the effect of beam energy on deformation. Figure 5d shows SEM and TEM micrographs, respectively, of c-C[100] membranes with thickness $t_0 = 87$ nm implanted with different values of E_0 (see figure S16 for additional micrographs). Five different ion energies of 10, 15, 20, 25, and 30 keV were used with a fixed D_0 of $8 \times 10_7$ ions/point. As E_0 increases, the locations of bubble clusters shifted further away from the membrane edge along the z-axis and upward surface swelling was reduced. The shift in the location of bubbles can be explained by the increased He$_+$ penetration depth with increasing E_0. Correspondingly, peak locations of densities of He$_+$ and vacancies in the longitudinal direction shift deeper.[11,32]

In contrast to the monotonic shift in bubble location, $R_z|_{max}$ did not show a monotonic increase with E_0, instead decreasing from 492 nm to 386 nm as E_0 increased from 20 keV to 25 keV. The origin of this change in $R_z|_{max}$ with ion energy may be related to the following three physical processes as E_0 increases (see figures S17-19 for supporting data): (1) The ratio of electronic to nuclear stopping power decreases, resulting in increased simulated $R_{x,y,z}$ and a decrease in simulated sputter yield. (2) Densities and peak locations of He$_+$ and vacancies in the longitudinal direction decrease and increase, respectively. This fact implies that not only is greater delivery of He$_+$ required to coalesce nanobubbles into bubble clusters, but also larger bubbles are likely to be created. The dashed yellow circle in figure 5e shows that the maximum lateral width of bubble clusters increases as E_0 increases. (3) At a given $t_0 = 87$ nm, the probability of helium accumulation (P_{acc}) decreases, implying less damage. As E_0 increases, $R_{x,y,z}$ increases and the density of He$_+$ and P_{acc} decrease. Comparing these three processes with experimental results, we can explain the non-linearity as follows: the change in $R_z|_{max}$ follows the tendency of the first

23

process when $E_0 < 25$ keV. This is presumably due to reduced significance of P_{acc}, because most of the incident ions reside inside the membranes, *i.e.* P_{acc}^{SRIM} and P_{acc}^{IM3D} are over 0.92 and 0.88 when $E_0 < 20$ keV. The change in $R_z|_{max}$ follows tendencies of the second and third processes when $E_0 > 25$ keV. In this case, P_{acc} decreases abruptly from 0.92 to 0.81 (P_{acc}^{SRIM}) and from 0.88 to 0.78 (P_{acc}^{IM3D}), respectively. Furthermore, the density of He_+ reduces. Thus, more ions are required to reach the dose for nanobubble/bubble cluster nucleation, which is the key to promoting long-range ion-propagation, as stated previously in discussions of figure 4b-e. Thus, we concluded that an E_0 of 20 keV efficiently formed gas bubbles with the combination of intermediate values of P_{acc}, $R_{x,y,z}$, and He_+ density, resulting in the longest $R_z|_{max}$ in figure 5d.
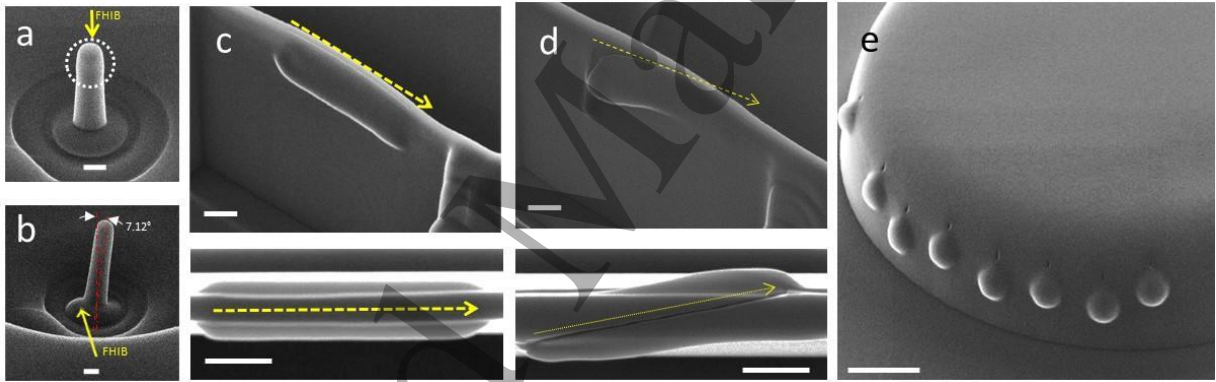
Figure 6. Control of nano-morphology *via* targeted ion irradiation of nanostructures; a nanoscale analogy to blow forming. (a) FHIB irradiation of a nano-pillar with a diameter of 100 nm. This image shows negligible deformation at the top of the pillar due to the absence of the geometric boundary. (b) FHIB irradiation at the boundary between a nano-pillar and its bulk substrate with a point exposure. The bulk substrate side forms a geometric constraint, which enabled deflection of the pillar in the opposite direction. In (a-b), irradiation conditions were 2.4 pA ion current, $E_0 = 30$ keV and $D_0 = 8.0 \times 10^6$ ions/point. (c) Cylindrical geometry embedded in flat vertical membrane wall with a line-scan (top: tilt view at 45° and bottom: top view). (d) Asymmetric cylindrical geometry embedded in flat nano-wall with a diagonal line-scan. In (c-d), the irradiation conditions were 2.4 pA ion current, $E_0 = 35$ keV and $D_0 = 8.0 \times 10^6$ ions/line. (e) Embedding nano-hemispheres in a micro-disk structure. A 35 keV FHIB was used to irradiate the edge of a micro-disk to form hemispheres at a regular interval. The depth variation with the same He_+ irradiation condition indicates not only the sensitivity of the location of exposed He_+ at the template structure but also the precision of the pre-patterned substrate.

24

Figure 6 shows advanced control of morphology by targeted He+ irradiation of nanostructures, which formed different geometric constraints. In the results described so far, we observed nano-spherical volume deformation on membrane walls, which is the result of internal gas pressure balanced by the constraining force of the material surface. Further, we confirmed that this volume deformation is dependent on D_0, t_0, E_0, and location in c-C, implying that we can control the volume deformation deterministically by controlling these parameters with the help of the geometric constraint provided by a controlled target. We interpreted our results as a nanoscale analogy to blow forming[62] induced by helium pressure inside and surrounding existing micro- and nano-targets.

Figure 6a shows minimal volume deformation formed in a nanopillar in contrast to the case when $t_0 = 100$ nm, which resulted in $t_d|_{max}$ of 230 nm as in figure 5a. This minimal volume deformation in the nanopillar is due to the absence of geometrical constraint and the high P_{esc}^{IM3D} of 0.40 in the pillar geometry. Figure 6b shows the use of geometrical constraint by FHIB irradiation at the boundary between a pillar and a bulk substrate, which acts as the geometrical constraint. We could deflect the nanopillar in a direction opposite to where p_i formed at the boundary. Furthermore, we also formed larger and more complex features in order to show the nanofabrication capabilities of He+-assisted blow forming.

Figures 6c-d show the results of He+ irradiation of a membrane with two different line-scan directions. Figure 6c shows the cylindrical geometry of a nanocavity with uniform volume deformation in the y-axis along the x-axis. In this case, a geometric constraint formed uniformly along the x-direction because we fixed the y-position of the FHIB at the centerline of the membrane. Figure 6d shows an example of using the line-scan in a diagonal direction on top of

25

the membrane. As the FHIB moves diagonally, the geometrical constraint changes, resulting in an asymmetric cylindrical geometry formed in the membrane.

Figure 6e shows an example of using the point-exposure in a micro-disk fabricated by FGIB. We performed the FHIB irradiation along the edge of the micro-disk of radius 5.50 μm, but with two slightly different radial locations of about 5.50 μm and 5.53 μm. The different locations effectively formed different geometric constraints due to the limitation of shaping a 90° vertical wall based on the Gaussian tail of FGIB. Consequently, the FHIB formed hemispheres in slightly different vertical locations. This example shows a novel application of the FHIB to produce localized features in large patterns.

Conclusions

Targeted ion irradiation of nanostructures has been shown to be an effective method for nanoscale modification of materials via a combination of radiation damage, helium implantation, and phase transition leading to different material properties in the deformation region. Our method offers the unique capabilities of observing site- and nanostructure-specific damage induced by targeted ion irradiation. We also present new He+-induced damage in nanostructures of c-C and c-Si that have not previously been reported. Specifically, the FHIB irradiation of c-C nanostructures exhibited extended damage due to long-range ion propagation and plastic deformation. Our study revealed that the extended damage was the result of dynamic changes associated with stopping power, phase transition, mass density, bubble nucleation/growth, and helium leakage. We have explained the role of material, ion dose, crystal orientation, dimension (thickness), and ion energy in nanostructure-specific He+-induced damage using electron microscopy and spectroscopy, and Monte Carlo simulations using SRIM and IM3D. Additionally, we have shown radiation damage

in nanostructures to be influenced by other irradiation conditions, such as ion species, exposure method, and location. We have also demonstrated the deterministic control of morphologies at the nanoscale via targeted He+ irradiation in existing micro- and nano-structures.

Although our investigation showed many advantages in the observation of He+-induced morphological changes, a full understanding of He+ interaction with nanostructures is still limited by a number of dynamic changes in materials properties. These are dependent on geometry and difficult to quantitatively predict, such as density of deposited helium and changes in elastic modulus following amorphization. However, we anticipate that our method and results will enable new ways to investigate materials physics, locally functionalize materials, and fabricate nanostructures. Our results can potentially be used to manipulate the hardest material, diamond, locally for micro- and nano- electromechanical systems.[57]

(1)   Hedler, A.; Klaumünzer, S. L.; Wesch, W. *Nat. Mater.* **2004**, *3*, 804.

(2)   Moon, M.-W.; Lee, S. H.; Sun, J.-Y.; Oh, K. H.; Vaziri, A.; Hutchinson, J. W. *Proc. Natl. Acad. Sci. U. S. A.* **2007**, *104*, 1130.

(3)   Liontas, R.; Gu, X. W.; Fu, E.; Wang, Y.; Li, N.; Mara, N.; Greer, J. R. *Nano Lett.* **2014**, *14*, 5176.

(4)   Kumar, N.; Kumar, R.; Kumar, S.; Chakarvarti, S. K. *Radiat. Phys. Chem.* **2016**, *119*, 44.

(5)   Shang, L. Y.; Zhang, D.; Liu, B. Y. *Phys. E* **2016**, *81*, 315.

(6)   Ronning, C.; Borschel, S.; Geburt, S.; Niepelt, R.; Muller, S.; Stichtenoth, D.; Richters, J.-P.; Dev, A.; Voss, T.; Chen, L.; Heimbrodt, W.; Gutsche, C.; Prost, W. *Phys. Status Solidi B* **2010**, *247*, 2329.

(7)   Hoffmann, S.; Bauer, J.; Ronning, C.; Stelzner, T.; Michler, J.; Ballif, C.; Sivakov, V.; Christiansen, S. H. *Nano Lett.* **2009**, *9*, 1341.

(8)   Möller, W.; Johannes, A.; Ronning, C. *Nanotechnology* **2016**, *27*, 175301.

(9)   Willke, P.; Amani, J. A.; Sinterhauf, A.; Thakur, S.; Kotzott, T.; Druga, T.; Maiti, K.; Hofsass, H.; Wenderoth, M. *Nano Lett.* **2015**, *15*, 5110.

(10)   Johannes, A.; Noack, S.; Wesch, W.; Glaser, M.; Lugstein, A.; Ronning, C. *Nano Lett.* **2015**, *15*, 3800.

(11)   Arora, W. J.; Sijbrandij, S.; Stern, L.; Notte, J.; Smith, H. I.; Barbastathis, G. *J. Vac. Sci. Technol. B* **2007**, *25*, 2184.

28

(12) Flatabo, R.; Agarwal, A.; Hobbs, R.; Greve, M. M.; Holst, B.; Berggren, K. K. *Nanotechnology* **2018**, *29*, 275301.

(13) Guo, Q.; Landau, P.; Hosemann, P.; Wang, Y.; Greer, J. R. *Small* **2013**, *9*, 691.

(14) Vuuren, A. J. van; Skuratov, V. A.; Uglov, V. V; Neethling, J. H.; Zlotski, S. V. *J. Nucl. Mater.* **2013**, *442*, 507.

(15) Ding, M.-S.; Du, J.-P.; Wan, L.; Ogata, S.; Tian, L.; Ma, E.; Han, W.-Z.; Li, J.; Shan, Z.-W. *Nano Lett.* **2016**, *16*, 4118.

(16) Jung, Y. J.; Homma, Y.; Vajtai, R.; Kobayashi, Y.; Ogino, T.; Ajayan, P. M. *Nano Lett.* **2004**, *4*, 1109.

(17) Robinson, A. P.; Burnell, G.; Sahonta, S.-L.; MacManus-Driscoll, J. *Adv. Eng. Mater.* **2009**, *11*, 907.

(18) Economou, N. P.; Notte, J. A.; Thompson, W. B. *Scanning* **2012**, *34*, 83.

(19) Winston, D.; Cord, B. M.; Ming, B.; Bell, D. C.; DiNatale, W. F.; Stern, L. A.; Vladar, A. E.; Postek, M. T.; Mondol, M. K.; Yang, J. K. W.; Berggren, K. K. *J. Vac. Sci. Technol. B* **2009**, *27*, 2702.

(20) Postek, M. T.; Vladar, A.; Archie, C.; Ming, B. *Meas. Sci. Technol.* **2011**, *22*, 024004.

(21) Joens, M. S.; Huynh, C.; Kasuboski, J. M.; Ferranti, D.; Sigal, Y. J.; Zeitvogel, F.; Obst, M.; Burkhardt, C. J.; Curran, K. P.; Chalasani, S. H.; Stern, L. A.; Goetze, B.; Fitzpatrick, J. A. J. *Sci. Rep.* **2013**, *3*, 3514.

(22) Scholder, O.; Jefimovs, K.; Shorubalko, I.; Hafner, C.; Sennhauser, U.; Bona, G.-L. *Nanotechnology* **2013**, *24*, 395301.

(23) Yang, J.; Ferranti, D. C.; Stern, L.; Sanford, C. A.; Huang, J.; Ren, Z.; Qin, L.-C.; Hall, A. R. *Nanotechnology* **2011**, *22*, 285310.

29

(24)   Fox, D. S.; Zhou, Y.; Maguire, P.; O'Neill, A.; Ó'Coileáin, C.; Gatensby, R.; Glushenkov, A. M.; Tao, T.; Duesberg, G. S.; Shvets, I. V; Abid, M.; Abid, M.; Wu, H.-C.; Chen, Y.; Coleman, J. N.; Donegan, J. F.; Zhang, H. *Nano Lett.* **2015**, *15*, 5307.

(25)   Gonzalez, C. M.; Timilsina, R.; Li, G.; Duscher, G.; Rack, P. D.; Slingenbergh, W.; van Dorp, W. F.; De Hosson, J. T. M.; Klein, K. L.; Wu, H. M.; Stern, L. A. *J. Vac. Sci. Technol. B* **2014**, *32*, 021602.

(26)   Wu, H.; Stern, L. A.; Xia, D.; Ferranti, D.; Thompson, B.; Klein, K. L.; Gonzalez, C. M.; Rack, P. D. *J. Mater. Sci. Mater. Electron.* **2014**, *25*, 587.

(27)   Huang, Z.; Li, W.-D.; Santori, C.; Acosta, V. M.; Faraon, A.; Ishikawa, T.; Wu, W.; Winston, D.; Williams, R. S.; Beausoleil, R. G. *Appl. Phys. Lett.* **2013**, *103*, 081906.

(28)   Cybart, S. A.; Cho, E. Y.; Wong, T. J.; Wehlin, B. H.; Ma, M. K.; Huynh, C.; Dynes, R. C. *Nat. Nanotechnol.* **2015**, *10*, 598.

(29)   Stanford, M. G.; Pudasaini, P. R.; Belianinov, A.; Cross, N.; Noh, J. H.; Koehler, M. R.; Mandrus, D. G.; Duscher, G.; Rondinone, A. J.; Ivanov, I. N.; Ward, T. Z.; Rack, P. D. *Sci. Rep.* **2016**, *6*, 27276.

(30)   Giannuzzi, L. A.; Prenitzer, B. I.; Kempshall, B. W. In *Introduction to Focused Ion Beams*; Giannuzzi, L. A., Stevie, F. A., Eds.; Kluwer Academic Publishers: Boston, 2005; pp 13–52.

(31)   Kashinath, A.; Demkowicz, M. J. *Model. Simul. Mater. Sci. Eng.* **2011**, *19*, 035007.

(32)   Livengood, R.; Tan, S.; Greenzweig, Y.; Notte, J.; McVey, S. *J. Vac. Sci. Technol. B* **2009**, *27*, 3244.

(33)   Stanford, M. G.; Lewis, B. B.; Iberi, V.; Fowlkes, J. D.; Tan, S.; Livengood, R.; Rack, P. D. *Small* **2016**, *12*, 1779.

30

(34)   Fox, D.; Chen, Y.; Faulkner, C. C.; Zhang, H. *Beilstein J. Nanotechnol.* **2012**, *3*, 579.

(35)   Li, R.; Zhu, R.; Chen, S.; He, C.; Li, M.; Zhang, J.; Gao, P.; Liao, Z.; Xu, J. *J. Vac. Sci. Technol. B* **2019**, *37*, 031804.

(36)   Hang, S.; Moktadir, Z.; Mizuta, H. *Carbon N. Y.* **2014**, *72*, 233.

(37)   Fairchild, B. A.; Olivero, P.; Rubanov, S.; Greentree, A. D.; Waldermann, F.; Taylor, R. A.; Walmsley, I.; Smith, J. M.; Huntington, S.; Gibson, B. C.; Jamieson, D. N.; Prawer, S. *Adv. Mater.* **2008**, *20*, 4793.

(38)   Sumant, A. V; Auciello, O.; Liao, M.; Williams, O. A. *MRS Bull.* **2014**, *39*, 511.

(39)   Hausmann, B. J. M.; Bulu, I.; Venkataraman, V.; Deotare, P.; Loncar, M. *Nat. Photonics* **2014**, *8*, 369.

(40)   Zalalutdinov, M. K.; Ray, M. P.; Photiadis, D. M.; Robinson, J. T.; Baldwin, W. J.; Butler, J. E.; Feygelson, T. I.; Pate, B. B.; Houston, B. H. *Nano Lett.* **2011**, *11*, 4304.

(41)   Kohn, E.; Gluche, P.; Adamschik, M. *Diam. Relat. Mater.* **1999**, *8*, 934.

(42)   Santori, C.; Barclay, P. E.; Fu, K.-M. C.; Beausoleil, R. G.; Spillane, S.; Fisch, M. *Nanotechnology* **2010**, *21*, 274008.

(43)   Chu, Y.; de Leon, N. P.; Shields, B. J.; Hausmann, B.; Evans, R.; Togan, E.; Burek, M. J.; Markham, M.; Stacey, A.; Zibrov, A. S.; Yacoby, A.; Twitchen, D. J.; Loncar, M.; Park, H.; Maletinsky, P.; Lukin, M. D. *Nano Lett.* **2014**, *14*, 1982.

(44)   Rugar, D.; Mamin, H. J.; Sherwood, M. H.; Kim, M.; Rettner, C. T.; Ohno, K.; Awschalom, D. D. *Nat. Nanotechnol.* **2014**, *10*, 120.

(45)   Bhallamudi, V. P.; Hammel, P. C. *Nat. Nanotechnol.* **2015**, *10*, 104.

(46)   Kruit, P.; Hobbs, R. G.; Kim, C.-S.; Yang, Y.; Manfrinato, V. R.; Hammer, J.; Thomas, S.; Weber, P.; Klopfer, B.; Kohstall, C.; Juffmann, T.; Kasevich, M. A.; Hommelhoff, P.;

31

Berggren, K. K. *Ultramicroscopy* **2016**, *164*, 31.

(47) McCloskey, D.; Fox, D.; O'Hara, N.; Usov, V.; Scanlan, D.; McEvoy, N.; Duesberg, G. S.; Cross, G. L. W.; Zhang, H. Z.; Donegan, J. F. *Appl. Phys. Lett.* **2014**, *104*, 031109.

(48) Ziegler, J. F.; Ziegler, M. D.; Biersack, J. P. *Nucl. Inst. Methods Phys. Res. B* **2010**, *268*, 1818.

(49) Li, Y. G.; Yang, Y.; Short, M. P.; Ding, Z. J.; Zeng, Z.; Li, J. *Sci. Rep.* **2015**, *5*, 18130.

(50) Reutov, V. F.; Sokhatskiĭ, A. S. *Techinical Phys.* **2003**, *48*, 68.

(51) Tan, S.; Klein, K.; Shima, D.; Livengood, R.; Mutunga, E.; Vladár, A. *J. Vac. Sci. Technol. B* **2014**, *32*, 06FA01.

(52) Fairchild, B. A.; Rubanov, S.; Lau, D. W. M.; Robinson, M.; Suarez-Martinez, I.; Marks, N.; Greentree, A. D.; McCulloch, D.; Prawer, S. *Adv. Mater.* **2012**, *24*, 2024.

(53) Evans, J. H. *J. Nucl. Mater.* **1977**, *68*, 129.

(54) Yang, Y.; Li, Y. G.; Short, M. P.; Kim, C.-S.; Berggren, K. K.; Li, J. *Nanoscale* **2018**, *10*, 1598.

(55) Khmelnitsky, R. A.; Dravin, V. A.; Tal, A. A.; Zavedeev, E. V; Khomich, A. A.; Khomich, A. V; Alekseev, A. A.; Terentiev, S. A. *J. Mater. Res.* **2015**, *30*, 1583.

(56) Bosia, F.; Argiolas, N.; Bazzan, M.; Fairchild, B. A.; Greentree, A. D.; Lau, D. W. M.; Olivero, P.; Picollo, F.; Rubanov, S.; Prawer, S. *J. Phys. Condens. Matter* **2013**, *25*, 385403.

(57) Battiato, A.; Lorusso, M.; Bernardi, E.; Picollo, F.; Bosia, F.; Ugues, D.; Zelferino, A.; Damin, A.; Baima, J.; Pugno, N. M.; Ambrosio, E. P.; Olivero, P. *Acta Mater.* **2016**, *116*, 95.

(58) Hlawacek, G.; Veligura, V.; van Gastel, R.; Poelsema, B. *J. Vac. Sci. Technol. B* **2014**, *32*,

020801.

(59)   Marshall, M. M.; Yang, J.; Hall, A. R. *Scanning* **2012**, *34*, 101.

(60)   Duan, H.; Xie, E.; Han, L.; Xu, Z. *Adv. Mater.* **2008**, *20*, 3284.

(61)   Timoshenko, S.; Woinowsky-Krieger, S. *Theory of plates and shells*, 2nd ed.; McGraw-Hill.

(62)   Ding, S.; Liu, Y.; Li, Y.; Liu, Z.; Sohn, S.; Walker, F. J.; Schroers, J. *Nat. Mater.* **2014**, *13*, 494.